PHYSICAL REVIEW E VOLUME 49, NUMBER 2 FEBRUARY 1994

Absolute and convective instabilities and noise-sustained structures in the Couette-Taylor system with an axial flow

Avraham Tsameret and Victor Steinberg
Department of Nuclear Physics, The Weizmann Institute of Science, Rehovot 76100, Israel

(Received 1 June 1993)

A detailed study of the Couette-Taylor system with axial flow in the range of Reynolds number Re up to 4.5, which is characterized by the propagating Taylor-vortices (PTV's) state, is presented. Two methods to measure the convective instability line are described. Comparative studies of the PTV's in the absolutely and convectively unstable regions are given. It was found that at $\mathrm{Re}<1$ the PTV's appear first at the outlet at the absolute instability transition. At $\mathrm{Re}>1$ the PTV's are also sustained in the convectively unstable region, but the properties of the PTV's in the absolutely and convectively unstable regions differ distinctively. In both regions the PTV's are characterized by the existence of an interface separating the pattern state from the Couette-Poiseuille flow. The interface is stationary in the absolutely unstable region and fluctuates in the convectively unstable region. The distance from the inlet to the interface changes as both control parameters $\bar{\epsilon}$ and Re are varied, where $\bar{\epsilon}$ is the distance from the convective line. This dependence is, however, different in both regions. In the absolutely unstable region the healing length is scaled with the PTV's group velocity at all values of $\bar{\epsilon}$ and Re, and diverges at the absolute instability transition line. In the convectively unstable region the healing length does not obey the general scaling but is about inversely proportional to $\bar{\epsilon}$. The most distinctive difference in the PTV's behavior in the two regions is a different sensitivity to noise. A time-dependent spatial profile of the PTV's leads to a broadband power spectrum of the velocity in the convectively unstable region near the outlet. The PTV's velocity power spectrum in the absolutely unstable region is, on the other hand, noise-free. The different sensitivity to noise was used as an experimental criterion to locate the absolute instability line for $\mathrm{Re}>1$. The wave-number selection is also found to be different in both regions. As a result, we concluded that the PTV's in the convectively unstable region are noise-sustained structures (NSS's) which were recently considered theoretically and observed in numerical simulations. The selective spatial amplification of an external noise and the characteristic dependence of the healing length on the control parameters and on the aspect ratio confirm our suggestion that the mechanism of NSS generation is a selective spatial amplification of a permanent noise at the inlet. An interaction of the noise with the NSS's leads to a noise modulation of the PTV's velocity.

PACS number(s): 47.20.−k, 47.60.+i, 43.50.+y

I. INTRODUCTION

The Couette-Taylor system has been traditionally used as a model system for the study of hydrodynamic instabilities and patterns formation in *closed* systems. Recently the Taylor system has become the focus of new interest as the application of a through flow in addition to the rotational flow has made it a useful system to study instabilities and the spatiotemporal dynamics of patterns in *open* flows. Two subjects, which appear to be significant for the formation and stability of patterns in open flow systems, are described in this paper. These subjects are the relation between absolutely and convectively instability conditions, and the role of noise in pattern formation in the convectively unstable region.

The distinction between absolute and convective unstable flows is important in hydrodynamic systems [1–10] and particularly in open flow systems. In the *convectively* unstable region perturbations grow only in their reference frame, affecting the basic flow locally but eventually are "blown out" of the system. In the *absolutely* unstable region, however, perturbations grow with time at any stationary point and therefore affect the flow everywhere. Examples of convectively unstable flows are parallel shear flow in a channel [7], plane Poiseuille flow, and jets in two and three dimensions [3]. Examples of absolutely unstable flow are the Rayleigh-Bénard convection, the Taylor vortex flow, temporal shear flow in a mixing layer [8], and also the well-known von-Karman vortex street in the near wake [10].

Although the distinction between absolutely and convectively unstable conditions is well established in hydrodynamics [6], the experimental study of the relation between these instability conditions was very limited until recently. Previous work [11–17] on the Taylor system with an axial flow was mainly concerned with the determination of the onset for periodic patterns in the presence of the through flow and with the classification of the various patterns. It was shown that for small Reynolds number Re the Couette-Poiseuille flow is stabilized and that the first instability is axisymmetric in the form of propagating Taylor vortices. Although the onset of axisymmetric patterns was measured in the small Re regime already by Snyder [11], the distinction between absolute and convective instabilities and the role of noise in open flow systems were never taken into account, and therefore the experimental results are not clearly understood. For example, Snyder reported [11] the measurement of the critical line for the onset of Taylor vortices in the presence of the through flow. It is not clear whether this line is the absolute or the convective instability line. Other numerical and experimental investigations of the Taylor system with an axial flow were carried out in wide-gap [16] and narrow-gap [17] geometries. These studies did not focus, however, on the small Re regime, $\mathrm{Re} < 4$, which was the subject of our studies.

Since the Couette-Taylor system with an axial flow enables one to conduct detailed and well-controlled experiments, it is an advantageous system to study quantitatively the properties of the patterns in the convective and absolute instability regions. The study of this system in view of the distinction between absolute and convective instabilities has been found [18–20] to contribute substantially to the understanding of open flow systems, as will be shown in this paper.

An important observation that was obtained in this study, to be presented below, is the existence of patterns in the convectively unstable region, where no flow other than the basic Couette-Poiseuille flow is allowed. This phenomenon was recently encountered in other hydrodynamic systems as well [1,2,5,9]. Patterns in the form of traveling waves with temporal and spatial modulations were observed in the convectively unstable region in thermal convection of binary mixtures [2] and explained [22] as the result of a reflection from the lateral boundaries. Whereas reflection is important in closed systems, it turns out to be not very significant for open flow systems. When, however, a permanent noise exists in the system, it can lead to *noise-sustained structures* in the convectively unstable region in a process of a continuous spatial noise amplification. In numerical simulations of the complex Ginzburg Landau (CGL) equation with a permanent noise source at the inlet, noise-sustained structures have been observed [1] in the convectively unstable region. These structures were shown to exhibit a unique wavelength that was selected out of the uniform spectrum of the white noise at the inlet.

Recently the Taylor system with an axial flow has been shown [18–21] to be a paradigm to study the effects of noise in the convectively unstable region, as will be shown in this paper.

The paper is organized as follows. The theoretical background and predictions are presented in Sec. II. The experimental setup is described in Sec. III. The following sections present the experimental results. First the determination of the convective instability line is discussed (Sec. IV). Then the experimental observations referring to the propagating Taylor vortices (PTV's) state in the absolutely unstable region are described: the spatial properties and the wavelength behavior of the PTV's state are presented (Sec. V). We discuss then the noise-sustained structures in the convectively unstable region and the mechanism for their generation and describe the experimental determination of the absolute instability line (Sec. VI). Section VII summarizes the results.

II. THEORETICAL CONSIDERATIONS

The Couette-Taylor system with an axial flow is comprised of two concentric cylinders which can be rotated about their common axis and a superimposed through flow in the axial direction. We have been studying a system in which the outer cylinder, of radius R_2, is at rest. The inner one, of radius $R_1 = \eta R_2$, is rotated with angular velocity Ω. A fluid of kinematic viscosity $\nu \equiv \mu/\rho$ is contained in the annular region between the cylinders.

One control parameter of the system which governs the rotatory motion is the Taylor number, defined as

$$T = \frac{4\eta^2 d^4}{1-\eta^2}\left[\frac{\Omega}{\nu}\right]^2 , \tag{1}$$

where $d = R_2 - R_1$. An application of a through flow in the axial direction provides a second control parameter which is defined as the Reynolds number of the through flow $\mathrm{Re} = \bar{v} d/\nu$, where $\bar{v}$ is the averaged velocity of the axial flow.

The equations governing the motion of the fluid are the Navier-Stokes equations for the velocity field $\mathbf{U} = (U_r, U_\theta, U_z)$, where r, θ, and z are the radial, azimuthal, and axial coordinates, respectively,

$$\frac{\partial \mathbf{U}}{t} + (\mathbf{U}\cdot\nabla)\mathbf{U} = -\frac{1}{\rho}\nabla p + \nu\nabla^2\mathbf{U} , \tag{2}$$

and the continuity equation

$$\nabla\cdot\mathbf{U} = 0 . \tag{3}$$

At small T the flow is stable and axisymmetric, and can be calculated from the above equations. The solution is a superposition of the circular Couette-Poiseuille flow and the axial Poiseuille flow

$$U_r = 0, \quad U_\theta(r) = Ar + B/r ,$$

$$U_z(r) = \mathrm{Re}\frac{(r^2 + C\ln r + D)}{E} . \tag{4}$$

A, B are constants that are determined by the no-slip conditions on the walls and are given by

$$A = -\frac{\eta^2}{1-\eta^2}\Omega, \quad B = \frac{\Omega R_1^2}{1-\eta^2} .$$

The constants in U_z are

$$C = \frac{1+\eta}{(1-\eta)}\frac{1}{\ln\eta} ,$$

$$D = \frac{1+\eta}{(1-\eta)}\frac{\ln(1-\eta)}{\ln\eta} - \frac{1}{(1-\eta)^2} ,$$

$$E = -\frac{1}{2}\left[1 + \frac{1}{1-\eta}\left[\frac{2\eta}{1-\eta}\right] + \frac{1+\eta}{\ln\eta}\right] .$$

In the absence of a through flow a transition to a spatially stationary periodic pattern—the Taylor vortex flow [23]—occurs as T is increased above a certain critical value T_0. The Couette-Taylor system without through flow is reviewed elsewhere [24].

The superposition of a through flow, with a relatively small Re value, makes the Taylor vortices drift downstream, and the flow takes the form of PTV's. For large enough Re other periodic patterns are manifested in the system [11,13,14].

In the following we will use the reduced Taylor number

$$\epsilon=\frac{1}{2}\left[\frac{T-T_0}{T_0}\right]=(\Omega-\Omega_0)/\Omega_0 \ ,$$

as the rotatory control parameter, where Ω_0 is the critical rotation speed for the onset of vortices without through flow, corresponding to the Taylor number T_0. $\epsilon_c(\mathrm{Re})$ denotes the critical value of ϵ for the onset of PTV's in the presence of axial flow at some value of Re.

The Couette-Taylor system with axial flow can be modeled by the CGL equation

$$\tau_0(\dot{A}+SA')=\bar{\epsilon}(1+ic_0)A+\xi_0^2(1+ic_1)A'' -g(1+ic_2)|A|^2A \ . \quad (5)$$

The coefficients of the equation for $\eta=0.75$ are [20,25] (up to very small correction due to Re) $\tau_0=0.0379$, $\xi_0^2=0.0725$, $S=1.23\,\mathrm{Re}$, and g is of order unity [26]. The complex coefficients are very small and can be neglected. The exact values of the coefficients of the CGL equation are given in Appendix A. $\bar{\epsilon}$ is the distance from the convective line, defined as

$$\bar{\epsilon}\equiv\frac{\Omega-\Omega_c(\mathrm{Re})}{\Omega_c(\mathrm{Re})}=\frac{(\epsilon-\epsilon_c)}{(1+\epsilon_c)} \ , \quad (6)$$

where $\Omega_c(\mathrm{Re})$ is the critical rotation speed in the presence of an axial flow at some value of Re.

Conditions for convective and absolute instability

Consider a small spatially localized perturbation of a stationary state of some hydrodynamic system. The perturbation can be developed in time according to three possible scenarios [6]. If the state is *absolutely stable,* the perturbation will decay in time in any frame of reference. If the state is *absolutely unstable,* the edges, or leading fronts of the perturbation, move in time in opposite directions, and therefore the perturbation will grow at any given stationary point. If the state is *convectively unstable* the edges of the perturbation will move in the same direction, and therefore the perturbation will grow only in a moving frame of reference, but will decay at any given stationary point. In the absolutely unstable case, the perturbation will grow and saturate (because of nonlinear effects) to form a pattern.

The conditions for convective and absolute instability of a given flow are derived from the analysis of the spatial and temporal behavior of a perturbation of the flow. The system becomes convectively unstable when the maximal temporal growth rate of the perturbation, along a ray of constant x/t, becomes positive. This transition happens at $T=T_c(\mathrm{Re})$, or $\bar{\epsilon}=\bar{\epsilon}_c=0$ [1,3,4]. The convective instability line is therefore defined as the line $\bar{\epsilon}_c(\mathrm{Re})$. The convective instability line was calculated [20,25] to be

$$\epsilon_c=0.000\,381\,\mathrm{Re}^2 \ , \quad (7)$$

for the Taylor system with axial flow.

The linearized GL equation approximates the dispersion relation by an expansion to first order in $\bar{\epsilon}$ and to second order in $k-k_c$ where $\omega=\omega_r+i\omega_i$ and $k=k_r+ik_i$ are complex [27]

$$\omega=\omega_c+\tau_0^{-1}(-c_0+i)\bar{\epsilon}+S(k-k_c) +\tau_0^{-1}\xi_0^2(c_1-i)(k-k_c)^2 \ .$$

The condition for the absolute instability can be found using the dispersion relation [3,4]. Using the conditions $(d\omega/dk)|k_{\max}=0$ and $\omega_i(k_{\max})=0$, where $k_{\max}$ is found by the saddle point analysis, one gets

$$\bar{\epsilon}_a=\frac{S^2\tau_0^2}{4\xi_0^2(1+c_1^2)} \ . \quad (8)$$

For the parameters of the Taylor system with an axial flow (see Appendix A) one gets $\bar{\epsilon}_a=0.004\,95S^2$, or $\epsilon_a=0.007\,89\,\mathrm{Re}^2$.

One realizes immediately a direct analogy between the expression for the absolute instability line (8) and a front propagation solution. Indeed, Eq. (8) can be written as

$$S_s=2 \ , \quad (9)$$

where $S_s=S\tau_0\bar{\epsilon}_a^{-1/2}/(\xi_0\sqrt{1+c_1^2}\,)$ is a scaled group velocity. The relation (9) is found to be a crucial one in the problem of the selection of a state behind the front of a propagating pattern. The mechanism of the velocity and wavelength selection of a pattern which propagates into an initially unstable state was identified by the so-called "marginal stability conjecture" [28]. The wave number of the pattern behind the front is selected such that [29]

$$k=c\epsilon^{1/2}/\xi_0 \ , \quad (10)$$

where

$$c=\frac{(1+c_1^2)^{1/2}\pm(1+c_2^2)^{1/2}}{(c_1-c_2)} \ .$$

c_1 and c_2 are the coefficients of the CGL equation. c can be approximated for small c_1 and c_2 as $c=(c_1+c_2)/2$. The scaled group velocity of the selected state is given by Eq. (9). This criterion is obtained from the requirement that the propagation velocity of the front separating the stable and the unstable states is equal to zero [28,29].

The transition line between the convective and absolute instability regimes in the Couette-Taylor system with axial flow can be viewed as the line defining the marginal stability of the front separating the Couette-Poiseuille state and the PTV's. The front is stable if it outruns any perturbation [30], namely, if the perturbation velocity is smaller than the front velocity. Convective or absolute instability is then considered with respect to the front. In the absolutely unstable regime the perturbations grow ahead of the front, and thus the front becomes unstable and advances into the interior of the system. As a result, a steady pattern in the form of the PTV's is observed in the column. At the convectively unstable regime, on the other hand, the front is stable, and because it is moving downstream the PTV's are convected away with the front. On the transition line between the convectively and absolutely unstable regions the propagation velocity of the front is zero. The PTV's state is therefore convectively unstable for $S_s > 2$, and it is absolutely unstable for $S_s < 2$.

III. EXPERIMENT

The general scheme of the experimental setup is shown in Fig. 1. It consists of the Taylor system, which is composed of the Taylor column [32] and the axial flow modification, and the laser Doppler anemometer, which was the main measuring tool. Two columns were used in the experiments, with the aspect ratios $\Gamma = L/d = 54$ and 48 (L is the length of the working-fluid region), and radii ratios $\eta = r_1/r_2 = 0.707$ and 0.77, respectively. The radii of the outer cylinders were $R_2 = 2.685$ and 4.100 cm, and the radii of the inner cylinders were $R_1 = 1.900$ and 3.150 cm, respectively. The overall deviation from horizontality along the inner cylinder was about 0.02 mm, and the eccentricity was below 0.07 mm. The outer cylinders were made of perspex and were polished to obtain optical transparency.

The column was installed horizontally and was modified by an axial flow arrangement. The axial flow was driven by gravity in a closed loop, with the use of a pump. The average flow rate was measured by precise flow meters in the range from 2×10^{-3} to 1.5 cm/s with an accuracy of 1×10^{-4} cm/s. In order to make the axial flow as uniform as possible in the azimuthal direction, the fluid passed an inlet chamber before entering the working region between the cylinders. The inlet chamber was constructed with flow directors and a stainless-steel net with (0.25×0.25) mm^2 mesh size. The net was used as nonrotational lateral boundaries at both sides of the column. The working fluid was a mixture of glycerol in water. Typically, the fluid had a kinematic viscosity of $\nu = 3.0cS$, which corresponds to a mixture of 32.4% by volume of glycerol in water at 22 °C. The viscosity of the fluid was determined from tabulated data [31] and was checked by measurements with a commercial viscometer (Haake CV-100). The temperature of the fluid was maintained constant to a level of ±25 mK. The temperature stability was achieved by circulating water in a jacket around the column by the use of a commercial refrigerator-heater circulating system and by stabilizing the room temperature to within ±1 °C. Before entering the column, the fluid passed through a copper tube which was immersed in the circulator water basin, so that the axial flow was stabilized to the desired temperature at the inlet. The temperature was measured by Fenwal regulating thermistors, with a sensitivity of about 4 $k\Omega/$°C.

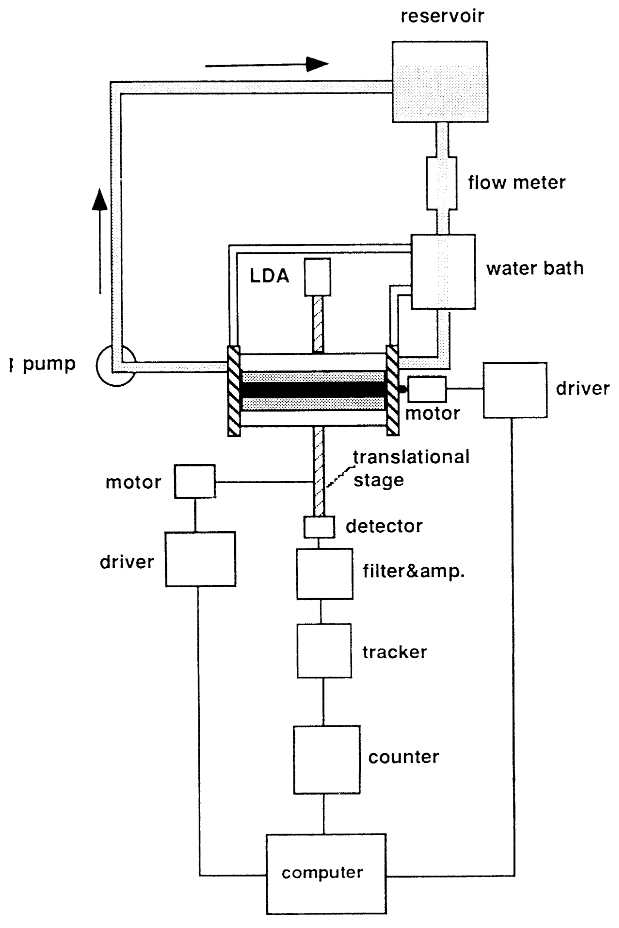

FIG. 1. The experimental setup. LDA stands for the laser Doppler anemometer.

The angular velocity of the inner cylinder was controlled by a stepper motor via a semirigid coupling. The motor was driven by a homebuilt electronic driver which is computer controlled. The accuracy of the averaged angular speed of the inner cylinder is better than ±0.05%.

Optical methods

The main measuring system was the laser Doppler anemometer (LDA), which enables an absolute and accurate measurements of the axial component of the velocity U_z. The LDA was built according to a design of Heinrichs *et al.* [33]. The optical setup in our system was the following. A 5-mW He-Ne laser is split into two beams with each beam passing through a Bragg cell. The Bragg cells shift the frequency of the laser radiation by 40.0 and 40.1 MHz, respectively, and these shifted components are then brought to a focus at their intersection point within the working fluid. The working fluid (a water-glycerol mixture) is seeded with 0.93-μm-diam polysterene latex spheres of concentration 4.2 μg/cc (6.5 particles/cc). This concentration exhibits an optimal signal to noise ratio, as was found in preliminary experiments. A sphere traveling with the local fluid velocity scatters light whose intensity is modulated at a frequency of 100 kHz$+v_z/\Delta x$, where $\Delta x \simeq 5$ μm is the fringe spacing. The light, which is scattered at a small angle (less than 10°), is collected using a Nicor 50-mm focal length lens which images the intersection volume on to a 400-μm-diam aperture. A phase-locked loop is used to track the instantaneous frequency of the current of a photodetector which is produced by the optical signal. The output of the tracker feeds a computer controlled counter which determines the frequency of the signal. The deviation of the modulation frequency from 100 kHz is proportional to the local axial velocity of the fluid. The LDA system is mounted on a Daedal translator which is controlled by a position controller.

In a complementary technique to the LDA, a flow visualization of the entire column was provided by adding 1% Kalliroscope solution [34] to the working fluid. An image of the column was obtained by means of a vidicon camera (RCA Model 2014x). The images were digitized and transferred to the computer for analysis, using an eight-bit frame grabber (Data Translation Model DT-2851) with a 512×512 spatial resolution.

IV. MEASUREMENT OF THE CONVECTIVE INSTABILITY LINE

A quantitative study of the system requires at first a precise determination of the convective instability line, which is denoted by

$$\epsilon_c(\mathrm{Re})=\frac{\Omega_c(\mathrm{Re})-\Omega_0}{\Omega_0} .$$

Here $\Omega_c(\mathrm{Re})$ is the critical rotation value for the onset of PTV's in the presence of the axial flow at some value Re and Ω_0 is the critical rotation value for the stationary case Re=0. Below this line the Couette-Poiseuille flow is absolutely stable, and no patterns exist. Above it, in the convectively unstable region, perturbations grow only in the comoving frame.

The measurement of the convective instability line was conducted by two methods. The first method [18] is based on the extrapolation of $\Omega_c(\mathrm{Re})$ from measurements of the PTV's velocity amplitude down to zero value. The velocity amplitude was measured as a function of Ω at various Re values, in the absolutely unstable region. The second method is the tracing of the spatial growth of an induced external perturbation.

A. Amplitude vs Ω measurements

A simple method to determine the convective instability line is to extrapolate measurements of the PTV's velocity amplitudes as a function of the control parameter Ω to zero amplitude values at various through-flow velocities. These measurements not only provide us with a method to obtain $\epsilon_c(\mathrm{Re})$, but also give us some insight with respect to the determination of the absolute instability line, as will be shown below.

The measurement procedure was the following. For a given Re value, Ω was increased quasistatically from below. At each Ω the axial velocity was measured near the outlet as a function of time with the LDA and the velocity amplitude which corresponds to the periodic component of the flow was deduced from a fit to the function $A\sin(\omega t+\phi)+V_0$. (V_0 corresponds to the through-flow velocity.) Before measuring we waited sufficient time in order to let the convective patterns to advect away. This waiting time was typically several longitudinal traverse times $\tau=(\Gamma/\mathrm{Re})\tau_v$, where $\Gamma=L/d$ and $\tau_v=d^2/\nu$ is the viscous diffusion time.

A plot of velocity amplitude vs. ϵ is given in Fig. 2 for the case without axial flow (Re=0) and for the case where a small axial flow is present (Re=0.61). The experimental data points are shown for Re=0 (open circles) and Re=0.61 (solid circles). The solid curve denotes the amplitude equation solution for the stationary (Re=0) system. In order to obtain Ω_0, the rotation speed that corresponds to the onset of the Taylor vortices in the stationary system, the data for the amplitude as a function of Ω was fitted to the GL equation of the Taylor system without axial flow. The procedure for the onset determination of the Taylor vortices in the stationary system was suggested by Dominguez-Lerma, Cannell, and Ahlers [32]. The theoretical critical Taylor numbers for the onset of the Taylor vortices without axial flow were interpolated from the calculations of Dominguez-Lerma [35] and were found to be $T_0=4424.2$ and 4116.0 for the aspect ratios $\eta=0.707$ and 0.77, respectively.

Upon the application of even a small through flow to the system, the curve of amplitude vs ϵ exhibits a qualitative change, as is seen in Fig. 2. First, the rounding at small ϵ, which is induced by finite size of the system, disappears. This fact suggests that the Ekman vortices near the boundaries do not affect the PTV's. This suggestion will be examined in more detail later. Second, the velocity amplitude becomes nonzero for a finite value of $\epsilon>0$ (which is $\epsilon\simeq0.004$ for the case presented in the figure). The jump in the amplitude demonstrates the fact that the system is convectively unstable for small values of ϵ. In the convectively unstable region the PTV's are advected away from the system and therefore zero velocity amplitude is measured in the stationary laboratory frame. The value of $\epsilon=\epsilon_s$, for which a transition in the velocity amplitude occurs, corresponds to a transition to the absolutely unstable region. ϵ_s, which is plotted below vs Re in Figs. 15 and 24, was found to coincide with the predicted value of the absolute instability line for Re < 1 and was found to strongly deviate from the absolute in-

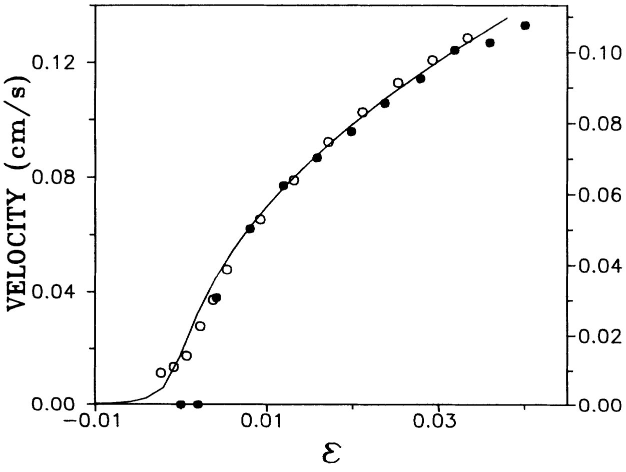

FIG. 2. Amplitude of the axial velocity vs ϵ for two sets of data, measured near the outlet boundary: open circles without through flow, and solid circles for Re=0.61 (velocity values on the left- and right-hand sides, respectively). The solid line is a fit to the GL equation for the stationary system. $\eta=0.707$.

stability line for Re > 1. It will be shown below that this discrepancy can be explained by noise-sustained structures which are manifested in the system for Re > 1. It is our interest here though to use the velocity amplitude vs Ω data of the PTV's in the absolutely unstable region in order to deduce the convective instability value ϵ_c. This was carried out by fitting the data of the velocity amplitudes with the solution of the GL equation

$$\bar{\epsilon}A - gA^3 = 0 \ , \tag{11}$$

which is $A = \sqrt{\bar{\epsilon}/g}$. The spatial derivatives in Eq. (11) are neglected because the measurements were carried out in the point which is located far enough from the lateral boundaries so that the flow was spatially uniform in the vicinity of the measuring point. The temporal derivative is neglected because we let the transients to die out before taking the measurement.

The critical value for the onset of vortices, $\epsilon_c(\mathrm{Re})$, is obtained from the fit. This procedure was carried out for several values of Re. The extrapolation of $\epsilon_c(\mathrm{Re})$ by this method becomes, however, less accurate as Re becomes larger due to the extrapolation involved in the fitting procedure.

B. Tracing a generated perturbation

A method which directly measures the convective instability line is the generation of a perturbation at the inlet boundary and detection of the pulse amplitude near the outlet. This method for the Couette-Taylor system with a through flow was first proposed by Babcock, Ahlers, and Cannell [20] and was proved to be more accurate than the method that was described above. The perturbation can be generated mechanically by either an abrupt rotation of the inner cylinder, as was done by Babcock, Ahlers, and Cannell [20], or by a sudden change of the inlet boundary location, the method used by us. We generated a pulse by moving the inlet boundary forward and backward at a distance of about $0.5d$. The duration of the imposed motion was about 10 s, below the viscous diffusion time of the system $\tau_v = 30.1$ s. We generated the pulse by using a device that was built for this purpose, which was controlled by a stepper motor. The pulses were checked to be reproducible. A propagation of a generated perturbation is demonstrated in Fig. 3. The pulse is initially confined to within one or two vortex wavelengths, and after a short response time of the system the perturbation spreads spatially and grows in amplitude. In order to determine ϵ_c the pulse amplitude was measured with the LDA as it passed the point $z = 40d$ from the inlet. A typical plot of the pulse amplitude in time is presented in Fig. 4, for Re=3.41 and $\epsilon = 0.0164$. By reducing ϵ, smaller and smaller amplitudes could be detected. At small ϵ the signal was obscured by the noise. The signal was observed by a peak in the power spectrum, after Fourier transforming the data. The onset of convective instability $\epsilon_c(\mathrm{Re})$ was determined to be the value of ϵ for which the power spectrum exhibited no peak.

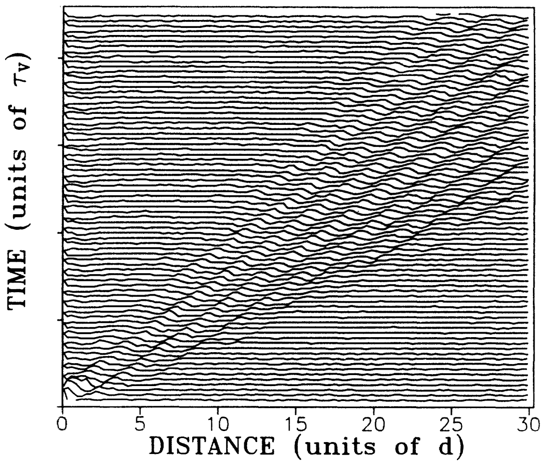

FIG. 3. The growth of a perturbation in the convectively unstable region. The pulse was generated by a sudden movement of the inlet boundary back and forth. Re=6.0 and $\epsilon = 0.0477$. $\eta = 0.77$.

The determination of ϵ_c can also be obtained by measuring the spatial growth of the pulse amplitude. A perturbation, generated at the inlet boundary, is amplified and expands during the propagation downstream. Assuming an initial Gaussian perturbation, $F_0(x) = A\exp(-\alpha x^2)$, it can be shown [1] that the subsequent evolution of the perturbation amplitude is given by

$$F(x,t) = A\frac{\exp(\bar{\epsilon}/\tau_0)t}{[1+4\alpha(\xi_0^2/\tau_0)t]^{1/2}} \times \exp\{-\alpha(x-St)^2/[1+4\alpha(\xi_0^2/\tau_0)t]\} \ , \tag{12}$$

where τ_0, S, $\bar{\epsilon}$, and ξ_0 are the parameters of the GL equation. Measurements of the pulse amplitude as a function of time and position, and fitting the data to a Gaussian function, yield therefore information about the growth rate of the perturbation. In order to extrapolate ϵ_c one has to carry out these measurements for several values of Ω, the rotation speed of the inner cylinder.

The measurement was carried out as follows: for a

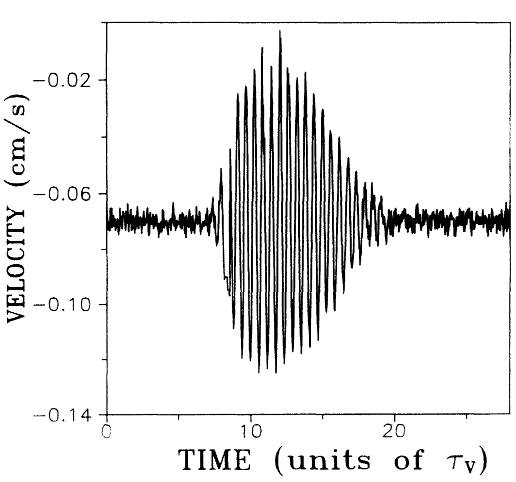

FIG. 4. Velocity vs time for a single pulse in the convectively unstable region. The pulse was generated at the inlet, and was observed at $z = 40d$. Re=3.41 and $\epsilon = 0.0164$. $\eta = 0.77$.

given Re and Ω a pulse was generated at the inlet, and the LDA monitored the axial velocity in time at a fixed position. This procedure was repeated at successive distances from the inlet. Figure 5 shows a typical curve of the pulse's velocity amplitude as a function of position, which was used in the determination of ϵ_c. Each data point corresponds to one experiment in which a single perturbation was generated, the axial velocity was recorded in time, and the maximal amplitude of the resulting pattern was evaluated. The natural way to evaluate the maximal amplitude of the pulse is to fit it to the function (12). This procedure, however, was not very reliable for pulses of a small amplitude, because of a poor signal-to-noise ratio. We therefore increased first the signal-to-noise ratio by autocorrelating the signal and deduced the maximal amplitude of the pulse from the zero-lag value of the autocorrelated signal. The details of this procedure are described in Appendix B.

Figure 5 demonstrates the fact that the amplitude A of the pulse grows spatially according to $A(x)=A_0\exp(\sigma x)$ where $\sigma=\bar{\epsilon}/(\tau_0 S)$ and A_0 is the initial amplitude of the perturbation. The solid line on Fig. 5 is an exponential fit from which the spatial growth rate σ can be obtained.

The growth rate σ as a function of the rotation speed Ω was deduced from similar measurements that were carried out for different values of Ω, at the same Re=4.72. The plot of σ as a function of Ω is shown in Fig. 6 for Re=4.72. The intersection of the fitted line with the Ω axis determines the critical rotation speed. We find $\Omega_c=0.8499$, a value which corresponds to $\epsilon_c(\mathrm{Re})=8.30\times10^{-3}$, in very good agreement with the predicted value $\epsilon_c(\mathrm{Re})=8.49\times10^{-3}$. The parameter τ_0 can also be deduced from the fit to the data in Fig. 6. We find $\tau_0=0.0327\pm0.0024$ (the theoretical value is $\tau_0=0.0379$).

As a result of the measurements the convective instability line was obtained, and it is shown in Fig. 7. The solid line is the theoretical line $\epsilon_c=0.000\,381\,\mathrm{Re}^2$ obtained from the linear stability analysis [20,25]. The points correspond to the data. The solid circles correspond to the data points obtained by measuring the pulse amplitude as a function of time near the outlet boundary. The open circle, depicted on the graph for Re=4.72, corresponds to the measurement of the spatial growth of the perturbation. It is seen that the different measurement procedures yield similar results. The agreement between the experimental data and the theoretical line is very good.

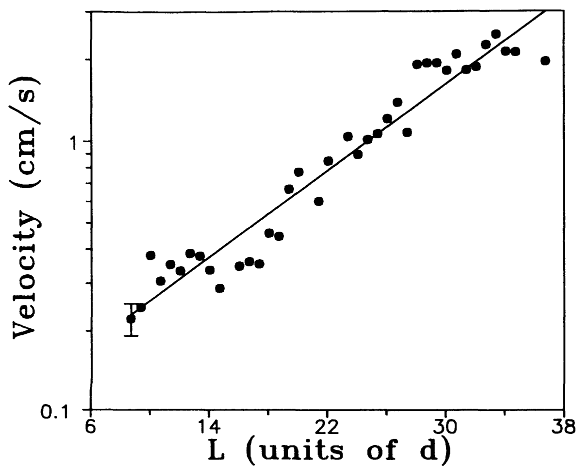

FIG. 5. The zero-lag amplitude of the autocorrelated pulses vs the distance from the inlet. (Re=4.72 and $\epsilon=0.0216$.) $\eta=0.77$. The fit gives σ, the spatial growth rate, which is used in the determination of ϵ_c(Re) (see text).

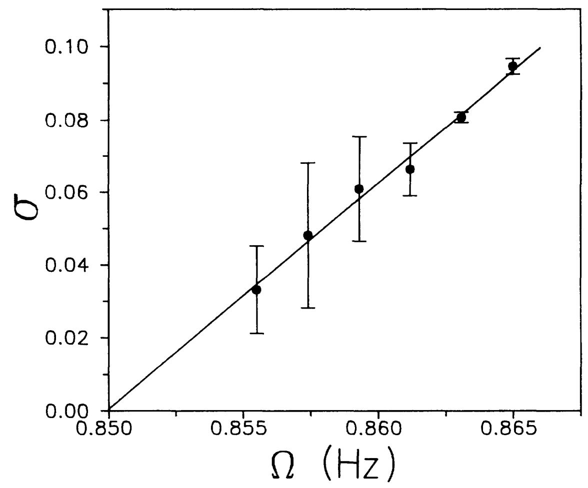

FIG. 6. The spatial growth rate σ vs the angular velocity of the inner cylinder, for Re=4.72. The intersection of the linear fit with the Ω axis gives $\Omega_c=0.8499$ Hz (the predicted value is 0.8501), which determines ϵ_c. $\eta=0.77$.

The open squares correspond to the data points obtained from the extrapolation of the fit to the amplitude equation, as described above. Most of the data points agree, within the error bars, with the theoretical line. For three data points with relatively larger values of Re a deviation from the theoretical line is observed. This devi-

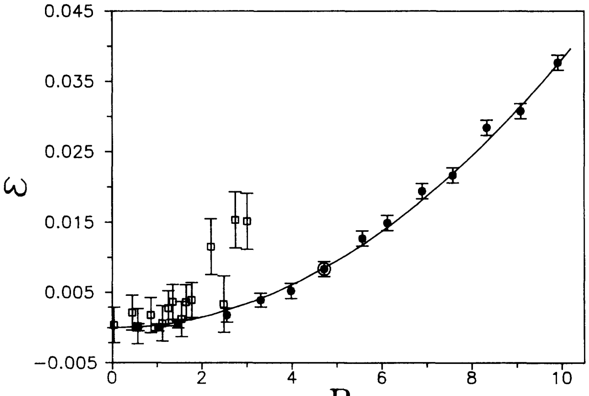

FIG. 7. The convective instability line. The solid line is the theoretical curve. The solid circles are the data obtained from the experiments with pulse generation, for $\eta=0.77$. At Re=4.72 the data obtained by observing the pulse amplitude at the outlet (solid circle) is plotted together with the data obtained by analysis of the spatial growth (open circle). The open squares are the data obtained by extrapolation with the GL equation, for $\eta=0.707$.

ation from the theoretical line can be explained by the fact that the determination of ϵ_c was deduced by an extrapolation procedure. At larger Re the extrapolation becomes less accurate, and therefore less reliable, because nonzero velocity amplitudes are first observed at larger ϵ values.

After verifying experimentally the convective instability line we now turn to the discussion of the properties of the PTV's state. In the next section we will describe the PTV's state in the absolutely unstable region. The spatial properties of the PTV's and the wavelength behavior will be presented.

V. PTV's IN THE ABSOLUTELY UNSTABLE REGION

A. Spatial properties

The PTV's in the absolutely unstable region are characterized by a spatial variation of the amplitude. The PTV's state has an amplitude profile with a characteristic healing length L_h, defined as the length at which the velocity amplitude reaches a certain part of its maximum value. L_h is found to increase as ϵ is reduced, as illustrated in Fig. 8, where the scaled velocity amplitude of the PTV's (amplitudes are scaled with $\epsilon^{1/2}$) is plotted as a function of the distance from the inlet for different values of ϵ and at a fixed Re$=1.77$. On the other hand, at a fixed value of ϵ the healing length increases with Re. The profiles in Fig. 8 correspond to states in the absolutely unstable region. A complementary picture of the spatial profile in the absolutely unstable region, taken with the vidicon camera, is presented in Fig. 9. In this figure the intensity of the optical signal is plotted as a function of axial position, at successive time intervals. The solid line across the plot depicts the position of the interface between the PTV's on the right and the Couette-Poiseuille flow on the left. The figure clearly demonstrates again the fact that the interface in the absolutely unstable region is stationary.

In order to determine the interface position several methods were used. One method that was used in the analysis is the demodulation of the optical signal in order to eliminate the fast oscillations and to obtain the profile envelope. The interface position was determined as the point that corresponds to a value of the demodulated amplitude larger than some specified threshold. We used in the analysis also root-mean-square (rms) and integral methods, namely, the threshold was set to be a specified fraction of either the rms value of the velocity of the PTV's near the outlet or a fraction of the integral over the rms velocity along the column. The latter specification of the threshold was mainly used because it is less sensitive to spurious intensity variations.

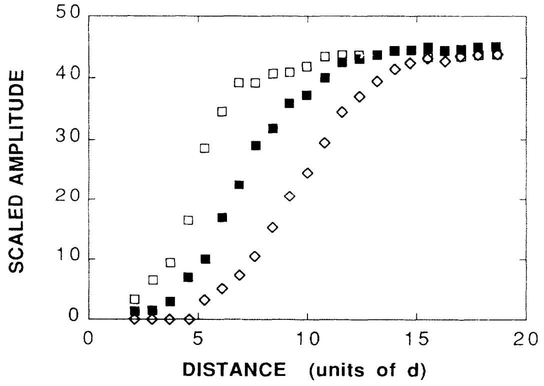

FIG. 8. Profiles of PTV's velocities $[A(\tau_0/\xi_0\sqrt{\overline{\epsilon}})]$ vs distance from the inlet in the absolutely unstable region, at Re$=1.77$ and $\overline{\epsilon}=0.042$ (open squares), $\overline{\epsilon}=0.034$ (solid squares), $\overline{\epsilon}=0.030$ (diamonds). $\eta=0.707$.

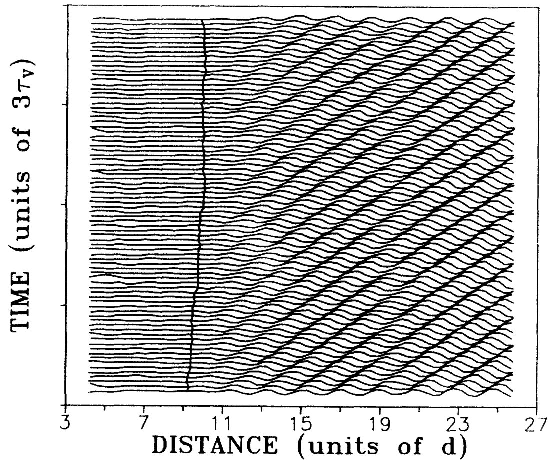

FIG. 9. Space-time contour plot of the optical signal intensity along the column for PTV's in the absolutely unstable region. The solid line across the plot defines the interface between the Couette-Poisseuille and PTV's states ($\epsilon=0.034$, Re$=2.2$, $\tau_v=d^2/\nu$). $\eta=0.77$.

Profiles of the velocity amplitudes in the absolutely unstable region were also observed in numerical studies of the Rayleigh-Bénard system with a through flow [36]. It was found that the healing length L_h increases as ϵ is reduced and diverges at the absolute instability line. The divergence of L_h was used as a criterion for the transition from the convective to the absolute unstable regime. A general scaling of the healing length $l_s=\overline{\epsilon}^{1/2}L_h/\xi_0$ as a function of a scaled group velocity $S_s=S(\tau_0/\xi_0)[\overline{\epsilon}(1+c_1^2)]^{-1/2}$ was suggested and verified numerically [36]. At $S_s=S_s^*=2$, which corresponds to the absolute instability line, l_s diverges.

This criterion was found to be valid in our system only for small Re, namely, for Re≤ 1 [18]. Figure 10 presents the results of the measurements of l_s vs S_s for different values of Re in our system. The data of different Re≤ 1 fall all on one curve that obeys

$$l_s=1.19(S_s^*-S_s)^{-0.6}\ . \tag{13}$$

The divergence of the healing length at $S_s^*=2$ is in agreement with the suggested criterion for the transition to the absolutely unstable region. The divergence of l_s can thus be taken as an experimental definition of the absolute instability line, for Re≤ 1. At Re>1, however, the above criterion is not satisfied as one finds finite values of l_s at $S_s>2$. The behavior of l_s at Re>1 manifests a discrepancy with the theoretical predictions which were

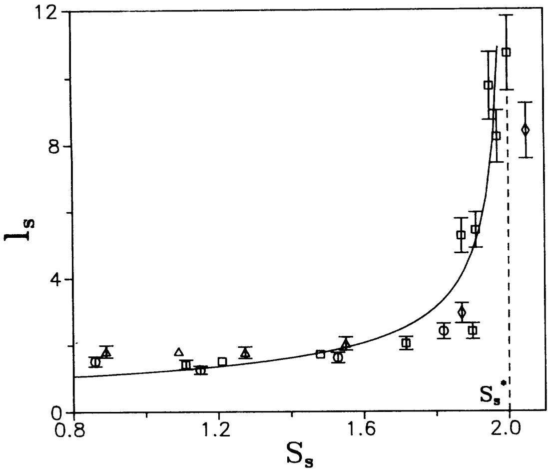

FIG. 10. The scaled healing length l_s vs the scaled velocity S_s. Circles, Re=0.56; triangles, Re=0.86; diamonds, Re=1.0; squares, Re=1.25. The solid line is a fit which gives $l_s=1.19(S_s^*-S_s)^{-0.6}$. $\eta=0.707$.

drawn from the study of the Rayleigh-Bénard system with an axial flow [36]. This discrepancy results from the fact that patterns are sustained in the convectively unstable region, as will be shown below. We note that the data at Re=1.25 > 1 are also included in Fig. 10.

Ekman vortices

We would like to point out here that so far we presented and discussed only the oscillatory component of the velocity field which corresponds to the periodic component of the measured signal. The spatial distribution of the oscillatory component of the velocity amplitude originates from the fact that at the lateral boundaries this component of the velocity amplitude is zero. It is an essential ingredient of the theory based on the GL equation for the oscillatory component of the velocity amplitude [36]. On the other hand, the full velocity field near the lateral boundaries is considerably more involved. Besides the oscillatory velocity amplitude, which plays the role of the order parameter of the bifurcation, there exists also an axial component of the velocity field due to the presence of an axial flow, and constant radial and axial components of the velocity field due to boundary effects. The latter causes the existence of the Ekman vortices in a classical Couette-Taylor flow. Of course simple one-component theory does not take into account these details. However, in order to complete the picture of the boundary conditions for the full velocity field and to understand an interplay and coexistence between constant radial and axial components of the velocity field, on the one hand, and the oscillatory velocity, on the other hand, we will describe our observations of the full velocity field in detail.

The application of a through flow to the Taylor system turns the system into an open one, and therefore one might think that the Ekman vortices, which are generated due to the presence of the rigid lateral boundaries [24], are washed away as soon as the axial flow is "switched on." It was found that this is not the case, as is demonstrated in Fig. 11. The velocity field of the Ekman vortices, composed of both the oscillatory component and the stationary component (which is obtained from the averaged velocity), is shown in this plot. The vertical lines denote the amplitude of the oscillatory component of the velocity field and the solid circles denote the averaged velocity values at every spatial point. Figure 11 demonstrates that the Ekman vortices modulate the oscillatory component of the velocity. The effect of the through flow on the Ekman vortices is illustrated by the plots on Fig. 12. In this figure the full velocity field near the inlet boundary is presented for a fixed Re=0.45 and different ϵ values (ϵ is increased from top to bottom). It is observed that the Ekman vortices always underly the flow pattern. The oscillating amplitude is decreased, and the shape of the vortices becomes less pronounced, as ϵ is reduced. The vortices, however, are not washed away by the through flow even for negative ϵ. Ekman vortices were observed for all Re < 4, a value at which a new mode of stationary spirals replaces the PTV's state. The Ekman profile for Re=3.0 (ϵ=0.054) is shown in Fig. 13. This figure shows that the spatial modulation is still observed for Re=3.0.

B. Wavelength measurements

The analogy between the PTV's state and a propagating front led us to suggest that the PTV's wavelength is uniquely selected according to the front propagating mechanism [18]. An additional motivation to study experimentally the wavelength behavior came from the results of numerical simulations that were applied to the Rayleigh-Bénard system with an axial flow [36]. The simulations showed a wavelength selection, so that the wavelength of the convection rolls was dependent only on the control parameters of the system, but was insensitive to the initial conditions.

The wave number of the PTV's in our system was mea-

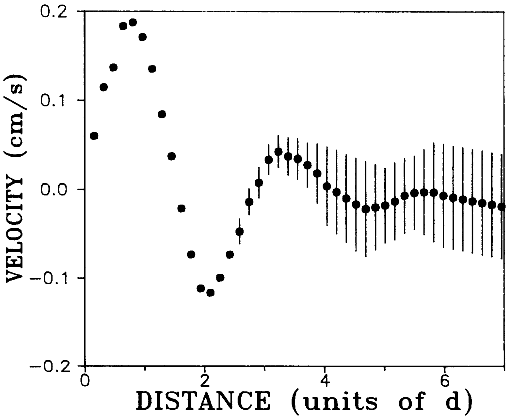

FIG. 11. The Ekman vortices in the presence of axial flow. The time-averaged axial velocity component (circles) and the velocity amplitude of the PTV's (bars) vs distance from the inlet for Re=0.45 and $\bar{\epsilon}$=0.0125 (measured at 0.2d from the inner cylinder). η=0.707.

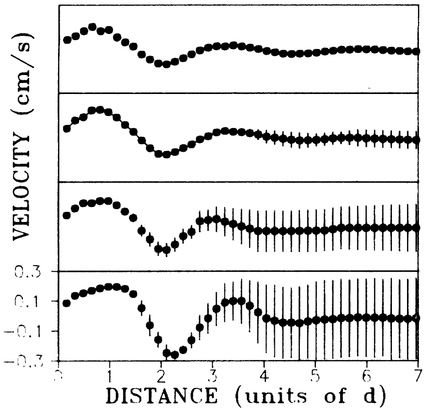

FIG. 12. The full velocity field near the inlet boundary. Re=0.45 and ϵ=0.1505, 0.0545, 0.0125, and −0.0035 (bottom to top). η=0.707.

sured using the vidicon camera. The wave-number measurements were carried out after waiting sufficient time [several longitudinal traverse times $\tau=(\Gamma/\mathrm{Re})\tau_v$] to allow the decay of wavelength variations along the column and after it was verified that no axial wavelength distribution was present. The bulk wave number of the PTV's was found to be uniquely selected by the through flow. The wavelength was found to be independent of the aspect ratio, initial conditions, and history of the system. An initial wave number that was prepared at Re=0 was changed to the selected wave number after the through flow was "turned on." The wave-number selection and its Re dependence is shown on Fig. 14. The open squares on the plot depict the wave number that was selected for the various values of Re. The solid symbols on the plot demonstrate the wave-number selection process. The initial wave number was prepared at Re=0 by quenching from the wavy mode state. Examples of three different initial wave numbers are shown by the different solid symbols (triangles, squares, and diamonds) at Re=0. The flow was then set for Re=0.9, and after sufficient time the different wave numbers collapsed to a single value.

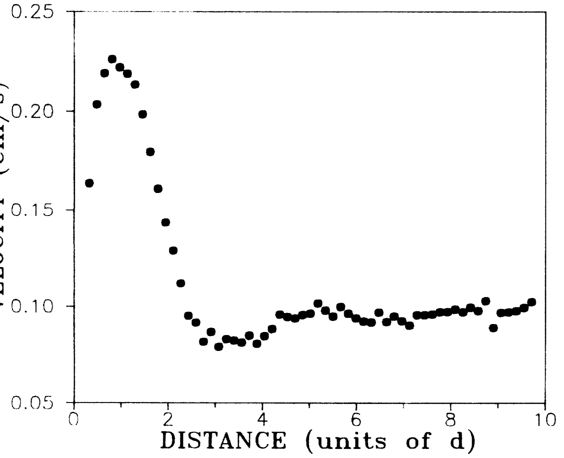

FIG. 13. The axial velocity vs distance from the inlet for Re=3.0 and ϵ=0.027. η=0.707.

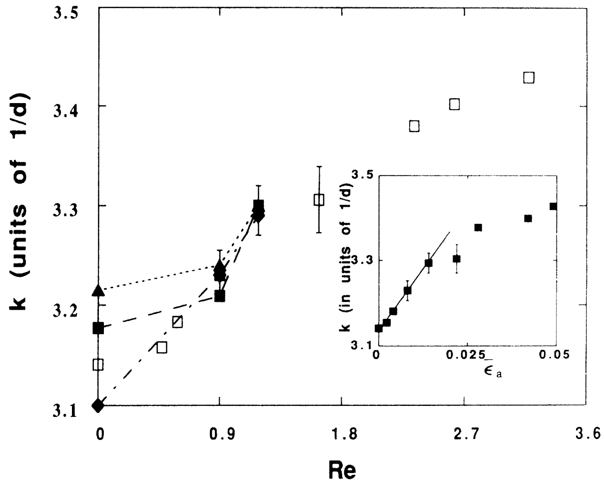

FIG. 14. The wavelength of the PTV's vs Re. Different symbols (diamonds, triangles, solid squares, and open squares) correspond to different initial states prepared with different k at Re=0. (Open square at Re=0 corresponds to k_c.) Dash-dotted, dotted, and dashed lines show the k-number selection process after the axial flow was applied. Inset: the wave number corresponding to states on the transition line, vs $\bar{\epsilon}_a$. The solid line is a fit to the data with Re ≤ 1. η=0.707.

The flow was then increased to Re=1.19, and a different wave number was selected. The wave number is increased with Re, as was found also for the Rayleigh-Bénard system with an axial flow [36]. No dependence of the wavelength on ϵ was observed.

The analogy between our system and the front propagation for Re < 1 suggests that the wavelength selection mechanism behind the front is similar to the wavelength selection in our system on the transition line $S_s=2$. The selected wave number behind a propagating front was calculated [29] to yield $k(\bar{\epsilon}_a)-k_c \simeq (c_1+c_2)\bar{\epsilon}_a^{1/2}/2\xi_0$, where c_1 and c_2 are coefficients of the CGL equation (5). Since c_1 and c_2 are proportional to Re in the first approximation (see Appendix A), we can write $c_1+c_2=n\,\mathrm{Re}$. Therefore

$$k-k_c \simeq n(\bar{\epsilon}_a/\tau_0)\ . \tag{14}$$

The wave number of the states on the transition line, i.e., with values of ϵ and Re that satisfy $S_s=2$, is presented in the inset of Fig. 14 as a function of $\bar{\epsilon}_a(\mathrm{Re})$. Note that the inset does not imply that there is a dependence of k on $\bar{\epsilon}$, but on $\bar{\epsilon}_a$, which is related to Re via the expression $S_s=2$. The data in the inset confirm qualitatively the linear scaling of k with $\bar{\epsilon}_a$, predicted by Eq. (14) for Re < 1, the regime of Re where the analogy with the front propagation holds. The experimental value of n, deduced from the slope for Re < 1, is $n=0.44$. This value is, however, about an order of magnitude larger than the theoretical value $n=0.028$.

We can conclude therefore that a wavelength selection exists for our system and that the mechanism of the front propagation can probably qualitatively explain the wavelength selection only for Re < 1. The mechanism for the wavelength selection for the noise-sustained structures (NSS's) in the regime Re > 1 is different and is unknown.

C. Onset of patterns

The initial assumption that PTV's are sustained only in the absolutely unstable region was suggested to be used as a criterion to locate experimentally the absolute instability line. If this assumption is correct, then the onset of patterns determines the absolute instability line. As will be shown here, this is the case only for $\mathrm{Re} < 1$. In order to determine the onset of patterns we used the procedure that was described in Sec. IV A. The amplitude of the PTV's was measured as a function of ϵ for a given Re, after waiting sufficient time to let convectively unstable patterns advect away from the system.

The resulting velocity vs ϵ plot was presented in Fig. 2 for $\mathrm{Re}=0.61$. The ϵ value above which PTV's are maintained in the system and below which no patterns are observed determines a point on the absolute instability line for $\mathrm{Re} < 1$. This ϵ value will be denoted by ϵ_s. A plot of ϵ_s as a function of Re, for the aspect ratio of $\Gamma=40$, is shown in Fig. 15. The solid line is the theoretical absolute instability line given by Eq. (8). The dashed line is the convective instability line given by Eq. (7). Region III, above the absolute instability line, is the *absolutely unstable* regime. The regime between the absolute and the convective instability lines is the *convectively unstable* regime. It is divided into two regions. In region I no patterns are observed and in region II patterns are sustained in the system. The circles denote ϵ_s for the onset of patterns observed. Figure 15 clearly demonstrates that the method described above [18] to measure the absolute instability line is correct only for small values of Re, namely, for $\mathrm{Re} \leq 1$. For $\mathrm{Re} > 1$, ϵ_s values were found [18] to be smaller than ϵ_a, the absolute instability value. This deviation means that patterns are observed in the "forbidden" convectively unstable region, contrary to the theoretical predictions. The existence of patterns in the convectively unstable region accounts for the discrepancies with the theory as was reflected in the behavior of the spatial profile and in the wavelength for $\mathrm{Re} > 1$.

It is important to note that the theoretical derivation of the conditions for the absolute and convective instabilities did not take into account the presence of noise in the system. In the following sections it will be shown that the intrinsic noise in the system is responsible for the existence of patterns in the convectively unstable region.

VI. NOISE-SUSTAINED STRUCTURES IN THE CONVECTIVELY UNSTABLE REGION

A close examination of the patterns in the convectively unstable region shows that they exhibit a noisy character which is not manifested by the PTV's in the absolutely unstable region. This noisy character is reflected in two ways, which are in fact two aspects of the same phenomenon. The first one is irregular fluctuations of the interface separating the PTV's from the Couette-Poiseuille flow and the second is a broad peak in the power spectrum.

A noisy character of the patterns in the convectively unstable region was first revealed by a measurement of the axial velocity as a function of time in the vicinity of the interface. Figure 16 shows a typical behavior of the velocity in time for $\mathrm{Re}=2.74$ and 1.55 [Figs. 16(a) and 16(b), respectively] near the interface. The time series was taken in region II on Fig. 15. It is seen that the amplitude exhibits irregular modulations in time. Note that the frequency of the modulations is larger for the larger Re. We will explain this point in Sec. VI D. An understanding of the amplitude modulations in time was obtained by the study of the temporal behavior of the PTV's spatial profile in the convectively unstable region.

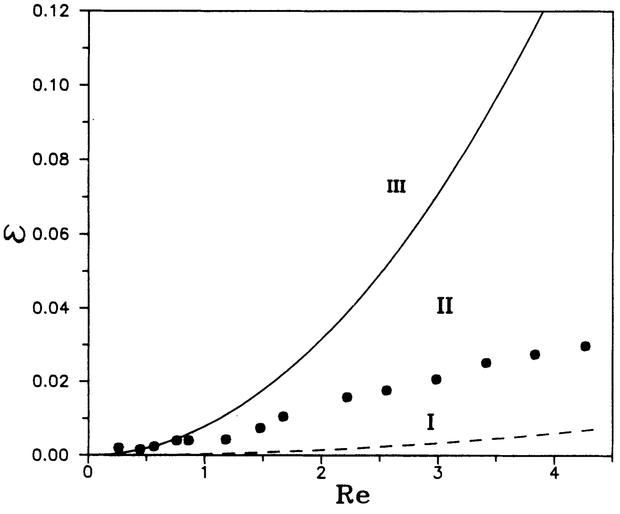

FIG. 15. The values of $\bar{\epsilon}_s$ for the onset of patterns (circles) vs Re, measured at $L=40d$. The dashed line is the convective instability line. The solid line is the theoretical absolute instability line above which the flow is absolutely unstable (region III). The data points determine the boundary between region I, where no patterns are present, and region II, where PTV's are observed. $\eta=0.77$.

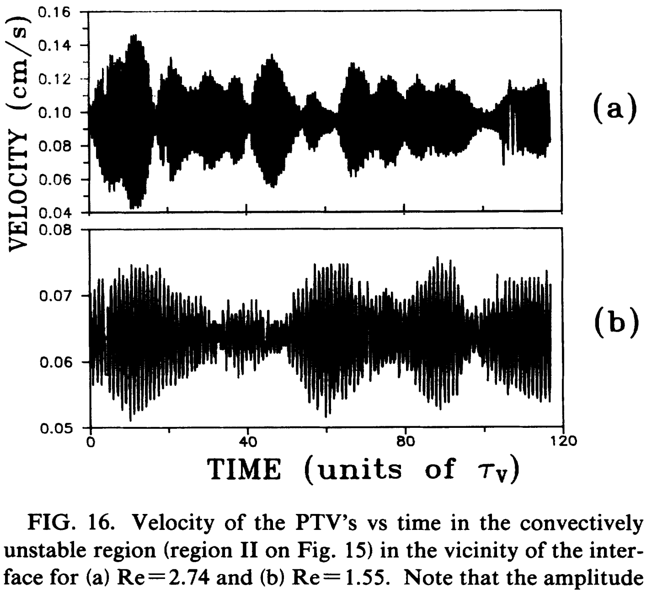

FIG. 16. Velocity of the PTV's vs time in the convectively unstable region (region II on Fig. 15) in the vicinity of the interface for (a) $\mathrm{Re}=2.74$ and (b) $\mathrm{Re}=1.55$. Note that the amplitude in (a) is more frequently modulated. [$\epsilon=0.0326$ (a) and 0.015 (b)]. $\eta=0.707$.

A. Spatial profile

It was found that in the convectively unstable region the interface between the PTV's and the Couette-Poiseuille flow exhibits time-dependent fluctuations, as demonstrated in Fig. 17. In this figure the intensity of the optical signal, obtained by the vidicon camera, is plotted as a function of axial position, at successive time intervals. The solid line across the plot depicts the position of the interface between the PTV's on the right and the Couette-Poiseuille flow on the left. The position of the interface was determined by the methods that were described in Sec. V.

A measurement of the velocity amplitude along the interface with the LDA is shown in Fig. 18, for Re$=2.5$ and $\bar{\epsilon}=0.03$. The measurement procedure was the following: for the given Re and ϵ we measured the axial velocity with the LDA along the column. Since the velocity amplitude of the PTV's is modulated in the convectively unstable region, then at every spatial point the velocity was recorded as a function of time for a period of time long enough to observe the velocity amplitude modulations. (This period of time was typically $30/f_0$, where f_0 is the PTV's frequency.) At every spatial point the maximum amplitude observed on the velocity time series was taken to correspond to this point along the profile. Figure 18 shows that the fluctuations of the interface are reflected in a larger scatter of the data points than the profiles in the absolutely unstable region (compare with Fig. 8 in the previous section).

A dependence of the interface position on ϵ for PTV's states in the convectively unstable region is shown in Fig. 19, for a fixed Re$=3.0$. This figure demonstrates the increase of L_h, the distance from the inlet to the interface position, as ϵ is decreased, as was found for the profiles in the absolutely unstable region (see Fig. 8). The dependence of L_h on $\bar{\epsilon}$ in the convectively unstable region for Re>1 is, however, quite different than what was found for the absolutely unstable region for Re<1. Figure 20 shows L_h as a function of $1/\bar{\epsilon}$ for Re$=2.7$. There is about a linear relationship between these variables, whereas a power-law dependence holds for the absolutely unstable region. Moreover, a general scaling of l_s as a function of S_s was shown to exist in the absolutely unstable region. Such a scaling does not exist in the convectively unstable region. The linear relationship between L_h and $1/\bar{\epsilon}$ will be explained below in Sec. VI D.

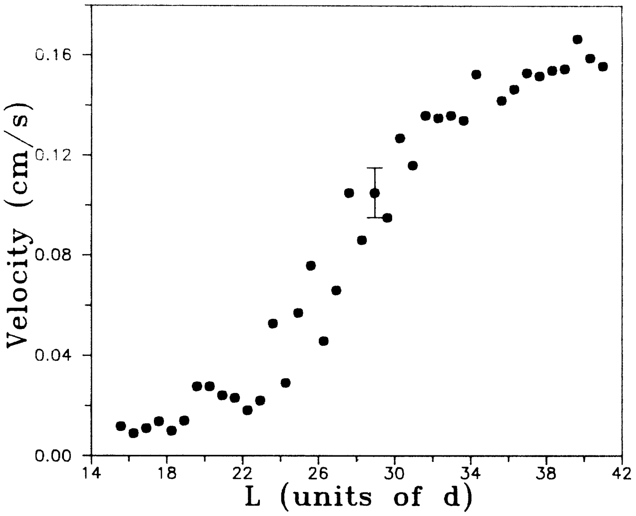

FIG. 18. The velocity amplitude of the axial velocity in the convectively unstable region (region II on Fig. 15) as a function of the distance from the inlet boundary. A typical error bar is shown. Note the scatter of the data, which is due to the fluctuations of the interface (Re$=2.5$ and $\bar{\epsilon}=0.03$. $\eta=0.77$.)

The interface fluctuations in the convectively unstable region were found to be irregular. As a result, the velocity amplitude near the interface is not constant but is rather modulated in an irregular fashion, as shown in Fig. 16 above. The direct connection between the interface dynamics and the amplitude modulations is demonstrated in Fig. 21. The interface position in time [Fig. 21(a)] is

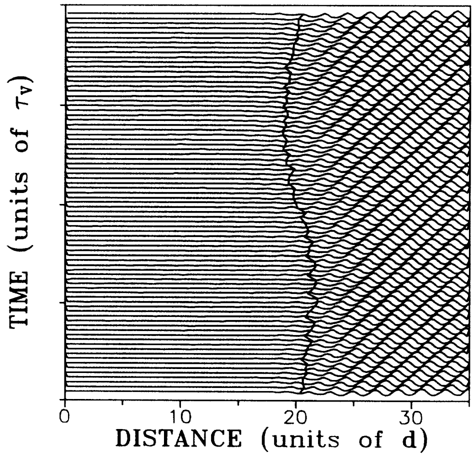

FIG. 17. Space-time contour plot of the optical signal intensity along the column for PTV's in the convectively unstable region (region II on Fig. 15). The solid line across the plot defines the interface between the Couette-Poiseuille and PTV's states ($\epsilon=0.04$ and Re$=3.0$). $\eta=0.707$.

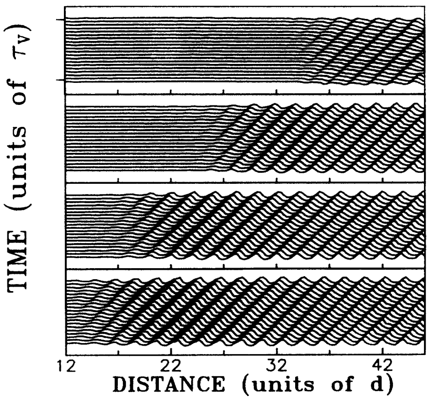

FIG. 19. Space-time contour plots for a fixed Re$=3.0$, and different ϵ values, demonstrate the increase in the healing length as ϵ decreases. $\epsilon=0.0246$, 0.0329, 0.0414, and 0.05 (from top to bottom). The plotted states correspond to region II on Fig. 15. $\eta=0.707$.

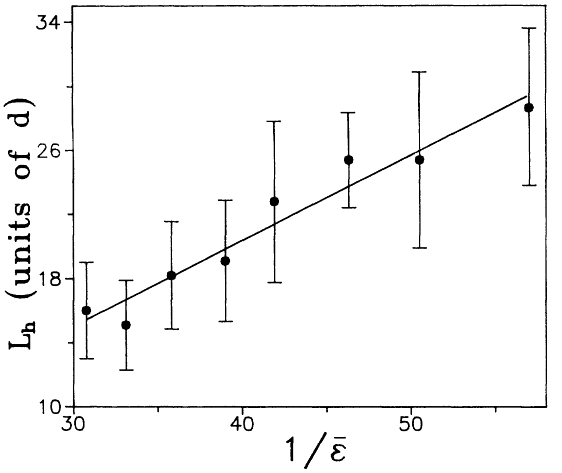

FIG. 20. The averaged interface position vs $1/\bar{\epsilon}$ in the convectively unstable region (region II on Fig. 15). The vertical bars show the range of the interface fluctuations (Re=2.7). The solid line is a linear fit to the data. The slope gives $\gamma=104$. $\eta=0.77$.

compared with the time-dependence of the PTV's velocity amplitude near the interface [Fig. 21(b)]. The amplitude in plot (b) was produced by demodulating the optical signal measured with the camera. The similarity between the temporal behavior of the interface and the PTV's amplitude is evident.

The noisy signature of the profile suggests that the patterns in the convectively unstable region are noise-sustained structures. In the absolutely unstable region, however, the amplitude is constant in time. Therefore, a criterion for the determination of the absolute instability line can be based on the difference in the PTV's temporal dynamics.

The following procedure was used to locate the absolute instability line. For a given Re, we recorded with the vidicon camera the intensity variations across the column as a function of time, for successive values of ϵ. The data were then analyzed in the following way: for each ϵ the interface position was identified, using the methods that were described above. The velocity variations in time for the points in the vicinity of the interface were then checked for an amplitude modulation. The ϵ value for which no amplitude modulations were observed along the column, for a given Re, was identified as the transition value between the convective and absolute instability regions.

B. Power-spectrum analysis

Another manifestation of the noise influence on the patterns dynamics in the convectively unstable region is reflected in the PTV's power spectrum. The temporal amplitude modulation that results from the noisy interface dynamics transfers into phase modulation of the PTV's near the outlet. The phase noise is manifested in a noisy power spectrum [19–21]. This observation is demonstrated in Fig. 22. Plots of the PTV's velocity amplitude as a function of time and their power spectra are shown, for a value of $\epsilon=0.0524$, in the convectively unstable regime and, for a value of $\epsilon=0.103$, in the absolutely unstable regime. In the convectively unstable region the velocity amplitude and power spectrum are shown for two locations, near the interface and close to the outlet. Their power spectra are qualitatively similar, although the time dependence of velocity amplitude is different: it is constant near the outlet, but it is irregularly modulated near the interface.

A more important conclusion from the plots is that the power spectra of the PTV's in the convectively and absolutely unstable regions are completely different—the

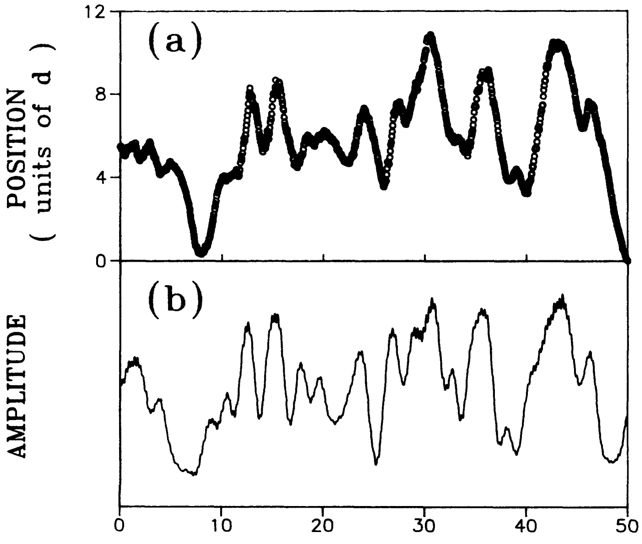

FIG. 21. (a) Interface position and (b) PTV's amplitude at a fixed location close to the interface in the convectively unstable region (region II on Fig. 15). ($\epsilon=0.034$ and Re=3.0.) $\eta=0.707$.

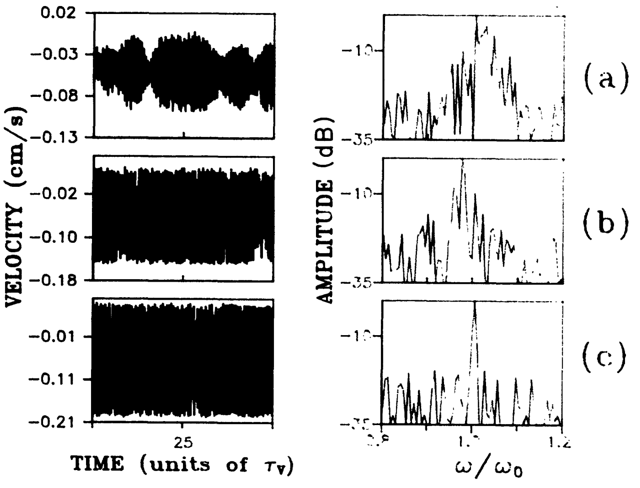

FIG. 22. Axial velocity of PTV's vs time and its time spectra. The data in (a) and (b) are taken in the convectively unstable region, at $\epsilon=0.0524$: (a) near the interface and (b) close to the outlet. The data in (c) are taken in the absolutely unstable region, at $\epsilon=0.103$. The peak frequency in the power spectrum is $\omega_0=10.8$. $\eta=0.707$.

broad peak in the convectively unstable region collapses to a sharp peak in the absolutely unstable region. This transition in the power spectrum can serve as another experimental criterion for identifying the absolute instability line [19,20]. We demonstrate the transition in the peak width in Fig. 23. The width can be characterized quantitatively [20] by the normalized variance of the peak in the power spectrum $\sigma^2 = \langle (f - \langle f \rangle)^2 / \langle f \rangle^2$. The angular brackets denote averaging over frequencies, which is obtained by integrating the frequencies in the vicinity of the main peak in the power spectrum.

The experimental procedure to determine the absolute instability line was as follows. For a given Re and ϵ, the axial velocity was recorded in time at a spatial point near the outlet, and sequences of typically 1024 data points, with 1-s intervals, were Fourier transformed to obtain the power spectrum. The value of ϵ for which σ^2 is minimal, a value that corresponds to the lowest ϵ value for which the power spectrum exhibits a sharp peak, was taken to be an experimental determination for the absolute instability line.

C. The stability diagram

The complete stability diagram of the system for PTV's is presented in Fig. 24. The lower solid line and the lower solid circles correspond, respectively, to the theoretical prediction and the experimental determination of the convective instability line, as described in Sec. V B. The upper solid line is the theoretical absolute instability line $\epsilon_a = 0.00789\,\mathrm{Re}^2$. The upper solid circles are the experimental data points for the absolute instability line, which were measured from the transition in the width of the power spectrum. The solid squares are the data points for the absolute instability line which were obtained from the measurements of the interface dynamics. The larger Re, the closer the interface to the inlet. At Re$\simeq$2.5 a new mode of stationary spirals appears near the inlet boundary, and an interaction between the PTV's state and the stationary spirals takes place. This interaction is probably another source for the modulation of the interface, which is manifested by the deviation of the solid squares data points from the absolute instability line.

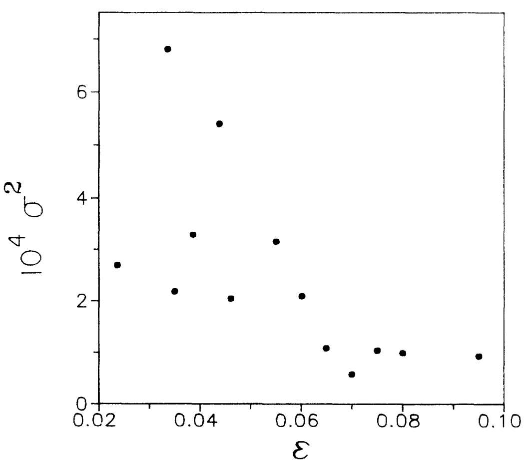

FIG. 23. The variance of the peak width in the power spectrum vs ϵ, at Re=3.0. The transition point is $\epsilon = 0.070 \pm 0.005$. (The predicted value is $\epsilon_a = 0.071$.) $\eta = 0.77$.

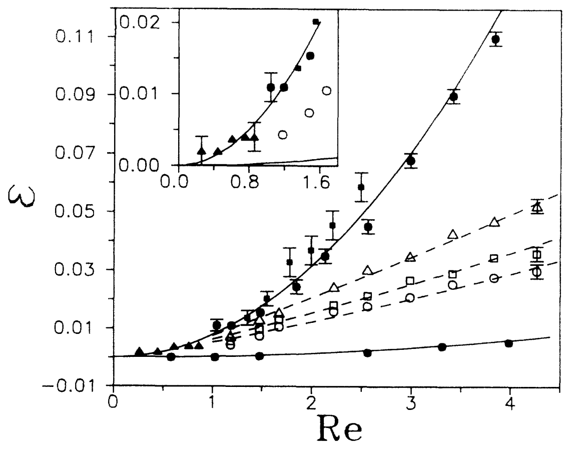

FIG. 24. The stability diagram for the PTV's. The lower solid line is the theoretical curve for the onset of the convective instability and the lower solid circles are the experimental data points. The upper solid line is the prediction of the GL equation for the absolute instability line and the solid symbols are the experimental data deduced from the width of power spectrum (solid circles) and interface fluctuations (solid squares). The solid triangles correspond to ϵ_s for Re < 1, which coincide with ϵ_a. The open symbols denote the experimental observation for the onset of patterns at downstream distances $z/d = 20$ (triangles), 30 (squares), and 40 (circles). The dashed lines are the fit to Eq. (17), with $\gamma = 181$. Inset: a high-resolution plot for small values of ϵ vs Re. Typical error bars are shown.

The values of ϵ_s for different positions of the measuring probe are plotted as the open symbols. (Triangles, squares, and circles correspond to different downstream distances $z/d = 20, 30, 40$, respectively.) The solid triangles correspond to the values of ϵ_s measured [18] for Re < 1, which coincide with the values of ϵ_a in this Re regime. The presentation of the data in this form on the onset of NSS's was suggested in Ref. [20]. We would like to point out that this presentation and comparison with the theory is quantitatively equivalent to the presentation in Ref. [20] since both approaches are based on the linear solution of the GL equation.

The observations on the noisy signature of the patterns in the convectively unstable region make it evident that these patterns are noise-sustained structures. We will elaborate more on the mechanism of creation of these structures in the following subsection.

D. Mechanism

The existence of patterns in the convectively unstable region can generally be explained by two mechanisms. The first is based on a reflection of perturbations from the lateral walls [2,22] and the second is based on continuous spatial noise amplification [1]. The picture based on the reflection mechanism is as follows. Perturbations that are naturally generated in the system grow exponentially as $\exp(\bar{\epsilon}\Gamma / S\tau_0)$ during propagation along the column. Upon reaching the outlet boundary a portion r of the perturbation's amplitude will be reflected back to be amplified again. A balance between the gain due to the spatial growth and the loss due to the reflection gives an onset shift for the pattern

$$\epsilon_s = \tau_0 \Gamma^{-1} S \ln(1/r) \ . \tag{15}$$

The region $\epsilon_s < \epsilon < \epsilon_a$ is the convectively unstable region, in which patterns are sustained because of the reflection from the lateral boundaries. This mechanism was suggested [22] by Cross and was verified experimentally in a Rayleigh-Bénard convection of a binary mixture [2].

In order to check the possibility of reflection in our system we generated a single perturbation at ϵ value for which no patterns exist. The perturbation grew to form a PTV's train which traversed the column. Upon reaching the outlet boundary we did not observe any interference phenomena (that can be expected as the result of reflection), and after the last vortex left the system no reflected waves were left behind. Estimates of our visualization technique resolution gives for the reflection coefficient a value of $r \leq 0.005$. The lower onset line in Fig. 15 corresponds to $r = 0.0055$. This means that if the shift in the onset were due to reflection it would be observed. Moreover, according to the reflection mechanism a pattern is sustained in the system because it is partly reflected from *both* of the lateral boundaries after being amplified during advancing towards the boundaries. In all the experiments that we have performed we have never observed a pattern that propagated from the outlet to the inlet, in the direction opposite to the flow. Therefore, we conclude that the contribution of reflection to the patterns in the convectively unstable region can be considered as negligible.

The second mechanism to explain the patterns is the generation of noise-sustained structures in a process of permanent noise amplification. A perturbation that is generated spontaneously at the inlet is amplified, grows exponentially, and is saturated to form a pattern. In the convectively unstable region, a single perturbation will eventually be convected away from the system. In order to have a sustained pattern in the convectively unstable region an existence of a permanent source of noise in the system is necessary. The intrinsic noise of the system, whose origin will be discussed elsewhere [37], can serve as such a permanent source of perturbations.

The amplitude of the initial perturbation, denoted by A_i, is spatially amplified and the fastest growing mode grows to an amplitude $A(z) = A_i \exp(Cz)$, at a distance z from the inlet. The exponential growth is explained by the linear spatial growth of perturbations in the convectively unstable region. C can be derived by solving the linear part of the GL equation (5). The time-independent amplitude, resulting from a perturbation amplitude A_i at the inlet, is [1,36]

$$A(z) = A_i \exp\left\{ \frac{z}{\xi_0} [\bar{\epsilon}_a^{1/2} - \sqrt{\bar{\epsilon}_a - \bar{\epsilon}}] \right\} \ . \tag{16}$$

This equation can be written as a relation between $\bar{\epsilon}$ and S

$$\bar{\epsilon} = \tau_0 \Gamma^{-1} S \ln\gamma - (\xi_0 \ln\gamma / \Gamma)^2 \ . \tag{17}$$

The parameter $\gamma = A/A_i$ is defined as the ratio between the initial amplitude of a perturbation and the amplitude of the pattern at $z = \Gamma$. Thus, for a given S, $\bar{\epsilon}$ should exceed a threshold value in order to provide sufficient gain to sustain a structure, in a system with an aspect ratio Γ. Equation (17) shows that the threshold for the pattern formation $\bar{\epsilon}_s$ strongly depends on Γ. This is understood by the fact that the larger the aspect ratio, the longer the time the perturbations grow, and therefore a smaller ϵ is required in order to reach a saturated amplitude value.

In order to check Eq. (17) we measured ϵ_s, the value that corresponds to the onset of patterns in the convectively unstable region for various values of Γ in a range $1 < \mathrm{Re} < 4.5$, following a previous suggestion and measurements that were carried out by Babcock, Ahlers, and Cannell [20]. The velocity amplitude that was chosen to correspond to ϵ_s was about 10% from the amplitude value which was measured after the spatial profile of the PTV's state reached saturation. Variation of Γ can be done in two ways. One is by changing the working length of the column by advancing the inlet boundary towards the outlet, keeping the LDA in a position near the outlet. The second is by keeping the inlet boundary in place and changing the position of the LDA along the column. We used the second method in order not to alter the boundary conditions between measurements for different Γ. Plots of ϵ_s as a function of Re are shown on Fig. 24 for different positions of the LDA probe z/d. The circles, triangles, and squares correspond to $z/d = 40, 30, 20$, respectively. The larger z/d is, the larger the spatial amplification of the perturbation becomes. Therefore the patterns can be observed at a lower value of ϵ. Using Eq. (17), all the data points for different z/d can be fitted with only one fitting parameter, namely, γ. The dashed lines in Fig. 24 present the fit by Eq. (17) with $\gamma = 181$. As can be seen, the agreement between the data and the fit is very good, which means that the mechanism of noise-sustained structure can be correctly modeled by Eq. (17).

A simplified expression for the threshold of the patterns $\bar{\epsilon}_s$ can be obtained for $\bar{\epsilon} \ll \bar{\epsilon}_a$. Then one obtains [19] from Eq. (16) that

$$\bar{\epsilon}_s = \tau_0 \Gamma^{-1} S \ln\gamma \ . \tag{18}$$

The healing length of the interface for the patterns in the convectively unstable region is predicted by Eq. (18) to be inversely proportional to $\bar{\epsilon}$

$$L_h = \tau_0 \bar{\epsilon}^{-1} S \ln\gamma \ . \tag{19}$$

This relationship is valid only for the patterns in the convectively unstable region, namely, for $\mathrm{Re} > 1$. In Fig. 20, presented above, the averaged distance of the interface from the inlet L_h is plotted vs $1/\bar{\epsilon}$. The linear dependence, predicted by Eq. (19), is obvious. The general dependence of L_h on $\bar{\epsilon}$ is found by inverting Eq. (17). One obtains

$$L_h = \tfrac{1}{2} \tau_0 S \ln\gamma \bar{\epsilon}^{-1} \left[1 + \left[1 - \frac{4\xi_0^2}{S^2 \tau_0^2} \bar{\epsilon} \right]^{1/2} \right] \ . \tag{20}$$

A fit to the data presented in Fig. 20 with Eq. (20) gives for the amplification ratio $\gamma=104$. This value of γ is smaller than the one obtained from the fit by Eq. (17). The discrepancy can be explained by the fact that γ depends on L_h only logarithmically. The logarithmic dependence of γ on L_h and on $\bar{\epsilon}_s$ makes the estimation of the noise level in the system, which can be deduced from the value of γ, to be not a very reliable procedure. Furthermore, the large error bars due to the fluctuating interface increase the uncertainty in the determination of L_h.

The process of the continuous noise amplification results in the generation of a noise-sustained structure with an interface between the Couette-Poiseuille flow and the noise-sustained structures, as is demonstrated in Figs. 17–19. The interaction of the noise with the interface can explain the fact that the amplitude modulations in the vicinity of the interface are different at different Re values. As is demonstrated in Fig. 16, the larger Re is, the larger the amplitude modulation frequency becomes (or alternatively, the smaller the time between successive amplitude modulations becomes). This is made clear by the following picture: increasing Re makes the group velocity, by which the perturbation propagates, larger. Therefore, the larger Re, the more frequent the interaction of the perturbations with the interface becomes. Thus, since the perturbations are not correlated, the amplitude will be modulated more frequently at larger Re.

E. Frequency selection

The numerical simulations that were carried out by Deissler [1] on the CGL equation with a boundary noise have shown that the system selects a unique frequency out of the uniform spectrum of the noise. This frequency selection gives rise to a wave-number selection [1].

To demonstrate this frequency selection in our system we have carried out the following experiment. External noise with a uniform power spectrum was applied to the system in the convectively unstable region. The noise was applied to the inlet boundary by moving the mesh at the boundary in a random fashion. The details of the experiment are described elsewhere [37]. Before the application of the external noise, no patterns were observed in the column. After perturbing the system, noise-sustained structures appeared in the system. Pictures of the column were taken by the vidicon camera at successive time intervals and transferred to the computer. The data of the light intensity in time, for a given spatial point, were then Fourier transformed. This analysis was carried out for the spatial points along the system. In this way the power spectrum of the axial velocity was obtained along the column. Figure 25 shows the power spectrum along the column for Re=4.73 and $\epsilon=0.029$. Near the inlet boundary the spectrum is uniform due to the generation of perturbations at the inlet. As the distance from the inlet is increased to about $7d$ the uniform spectrum collapses to a single peak, which corresponds to the frequency ω_0. ω_0 is the natural frequency of the system, namely, it is the frequency of the PTV's that are sustained in the system at the same Re value, without external noise, and corresponds to the phase velocity of the PTV's at the given Re value and $k=k_c$, as follows from the linear stability. (The nominal value of ω_0 is 0.565 s^{-1}.)

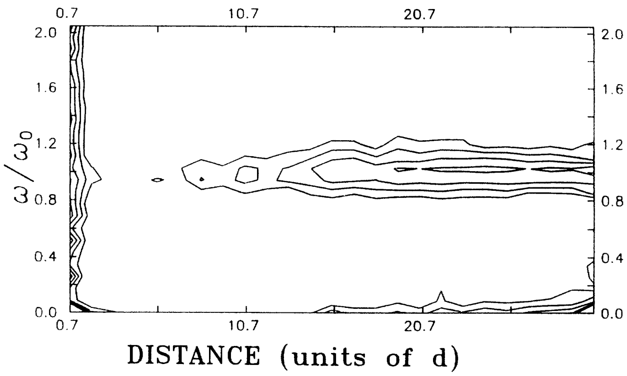

FIG. 25. The power spectrum along the column in the presence of external noise at the inlet boundary, in the convectively unstable region (region II on Fig. 15). Re=4.73 and $\epsilon=0.029$. $\omega_0=0.565\ \mathrm{s}^{-1}=14.6$ units of τ_v, is the natural frequency of the system. $\eta=0.77$.

VII. SUMMARY

A detailed study of the Taylor system with an axial flow in the range up to Re$\simeq$4.5 was presented in this paper. This system was found to be a convenient system for the study of instabilities in open flow systems and of the effect of noise on the formation of patterns in the convectively unstable region.

The methods to measure the convective instability line were described. The convective instability line was measured directly by generating a pulse at the inlet boundary and also indirectly from extrapolation of the PTV's velocity amplitude vs ϵ measurements. The experimental location of this line was shown to coincide with the theoretical prediction.

A comparative description of the PTV's properties in the convectively and absolutely unstable regions was presented. In the absolutely unstable region the PTV's are characterized as follows.

(i) The PTV's appear first at the absolute instability line at Re<1 (in contrast to the regime Re>1, where PTV's with different spatiotemporal properties appear first in the convectively unstable region).

(ii) The PTV's exhibit a spatial profile of the velocity amplitude. This profile is an interface which separates the PTV's state near the outlet from the Couette-Poiseuille flow near the inlet. The interface is stationary.

(iii) It was found, in accordance with the theory, that the distance from the interface to the inlet is scaled with the nondimensional group velocity of the PTV's for all ϵ and Re. The healing length of the interface diverges at the absolute instability line at Re<1.

(iv) The power spectra of the PTV's velocity is noise-free.

(v) The PTV exhibit a unique wave-number selection at given values of Re of the axial flow. This selection mechanism is probably related to the front propagating solution of the CGL solution.

The PTV's in the convectively unstable region are characterized as follows.

(i) At Re > 1 the PTV's are observed first in the convectively unstable region.

(ii) The PTV's sustained in the convectively unstable region also exhibit an interface separating the pattern state from the Couette-Poiseuille flow. The profile, however, is found to fluctuate. The fluctuations of the interface lead to a modulation of the velocity amplitude near the interface.

(iii) The healing length of the PTV's does not exhibit a general scaling. Instead, the distance from the inlet to the interface is about inversely proportional to $\bar{\epsilon}$.

(iv) The fluctuating interface leads to a phase noise which is manifested in a noisy power spectra of the velocity amplitude near the outlet, contrary to the noise-free spectra of the PTV's in the absolutely unstable region. The sensitivity of the PTV's to noise was used as an experimental criterion to locate the absolute instability line at Re > 1.

(v) A strong frequency selection and spatial amplification of perturbations was observed.

All these features of the PTV's lead us to the conclusion that the PTV's sustained in the convectively unstable region are noise-sustained structures, which were first found in numerical simulations by Deissler [1]. The mechanism of the NSS's was identified as a process of a permanent spatial noise amplification. The interaction of the noise with the NSS's leads to a noise modulation of the PTV's near the interface and to the noisy power spectrum near the outlet. The physical origin of the noise is the subject of another paper [37].

ACKNOWLEDGMENTS

We would like to acknowledge useful and helpful discussions with M. Lücke and R. Deissler. We thank M. Lücke and A. Recktenwald for providing us the results of the numerical calculations of the parameters of the CGL equation. This work was partially supported by the U.S.-Israel Binational Scientific Foundation Grant No. 90-00412, the Israel Science Foundation Grant No. 425/90-2, and the German-Israel Foundation Grant No. I-130091.

APPENDIX A: PARAMETERS OF THE SYSTEM

In this appendix the calculated [20,25] parameters of the Taylor system with an axial flow are summarized.

The CGL equation that describes our system is

$$\tau_0(\dot{A}+SA')=\bar{\epsilon}(1+ic_0)A+\xi_0^2(1+ic_1)A'' \\ -g(1+ic_2)|A|^2A \ . \tag{A1}$$

The coefficients of the CGL equation (for radii ratio $\eta=0.75$) are [25]

$$S=1.2296\mathrm{Re}+5.24\times10^{-6}\mathrm{Re}^3 \ ,$$

$$\tau_0=0.0379-2.42\times10^{-5}\mathrm{Re}^2+1.11\times10^{-8}\mathrm{Re}^4 \ ,$$

$$\xi_0^2=0.0725+4.78\times10^{-5}\mathrm{Re}^2+2.5\times10^{-8}\mathrm{Re}^4 \ ,$$

$$c_0=7.22\times10^{-3}-2.69\times10^{-6}\mathrm{Re}^3 \ ,$$

$$c_1=2.45\times10^{-2}\mathrm{Re}+4.93\times10^{-6}\mathrm{Re}^3 \ ,$$

$$c_2=3.48\times10^{-3}\mathrm{Re}+3.64\times10^{-7}\mathrm{Re}^3 \ .$$

The convective instability line

$$\epsilon_c=0.000\,381\,\mathrm{Re}^2+3.81\times10^{-8}\mathrm{Re}^4 \ .$$

The absolute instability line

$$\epsilon_a=0.007\,89\,\mathrm{Re}^2+6.31\times10^{-6}\mathrm{Re}^4 \ .$$

APPENDIX B: CORRELATION ANALYSIS OF PULSES

One of the methods to determine the convective instability line requires the analysis of pulses which are developed from a perturbation at the inlet boundary. Assuming an initial Gaussian perturbation at $t=0$, $F_0(x,t=0)=\overline{A}\exp(-\alpha x^2)$, the subsequent evolution of the envelope of the perturbation is given by [1]

$$F(x,t)=\overline{A}\frac{\exp(\bar{\epsilon}t/\tau_0)}{[1+4\alpha(\xi_0^2/\tau_0)t]^{1/2}}\exp\left[\frac{-\alpha(x-St)^2}{[1+4\alpha(\xi_0^2/\tau_0)t]}\right] , \tag{B1}$$

where τ_0, S, $\bar{\epsilon}$, and ξ_0 are the parameters of the GL equation.

We have measured the pulse velocity as a function of time, at a fixed spatial point. A suitable choice for a function to fit the data with is the following Gaussian function:

$$F_f(t)=A_1A_2\exp[-A_2^2(t-A_5)^2]\sin(A_3t+A_4) \ , \tag{B2}$$

where

$$A_1=(\overline{A}/\sqrt{\alpha})\exp(\bar{\epsilon}t/\tau_0),\ A_2=\sqrt{\alpha/[1+4\alpha(\xi_0^2/\tau_0)t]} \ ,$$

and $A_3=\omega_c$, the frequency of the PTV's at the onset.

In order to increase the signal-to-noise ratio the measured pulse was autocorrelated, using spectral analysis techniques [38]. The autocorrelation function which was considered is

$$C(\tau)=\int_{-\infty}^{\infty}F_f(t)F_f(t+\tau)dt \ . \tag{B3}$$

Integrating the right-hand side of Eq. (24), using the expression for $F_f(t)$ in Eq. (B2), yields

$$C(\tau)=\sqrt{\pi/8}A_1^2A_2\exp[-(A_2^2/2)\tau] \\ \times\{\cos(A_3\tau)-\exp[-A_3^2/2A_2^2] \\ \times\cos(A_3\tau+2A_4+2A_3A_5)\} \ . \tag{B4}$$

We have found that typically $A_3\simeq0.45$ and $A_2\simeq0.015$.

The second term on the right-hand side of Eq. (B4) is therefore of the order of 10^{-7} and can be neglected. Then, the autocorrelation function which was used for the fit is

$$C(\tau)=\sqrt{\pi/8}\,A_1^2A_2\exp[-(A_2^2/2)\tau]\cos(A_3\tau)\ .$$

From the fit the parameter A_1 was deduced. This procedure was repeated for a sequence of pulses, each of which was measured at a different spatial location. These measurements produced a plot of A_1 vs position, as is shown in Fig. 5.

[1] R. J. Deissler, J. Stat. Phys. **40**, 371 (1985); Physica D **25**, 233 (1987).

[2] V. Steinberg, J. Fineberg, E. Moses, and I. Rehberg, Physica D **37**, 359 (1989); P. Kolodner, C. Surko, and W. Williams, *ibid.* **37**, 319 (1989).

[3] P. Huerre, in *Instabilities and Nonequilibrium Structures,* edited by E. Tirapegi and D. Villaroel (Reidel, Dordrecht, 1987), p. 141; J. M. Thomas, P. Huerre, and L. G. Redekopp, Phys. Rev. Lett. **60**, 25 (1988).

[4] R. Tagg, W. S. Edwards, and H. L. Swinney, Phys. Rev. A **42**, 831 (1990).

[5] M. A. Schatz, R. P. Tagg, H. L. Swinney, P. F. Fisher, and A. T. Patera, Phys. Rev. Lett. **66**, 1579 (1991).

[6] L. D. Landau and E. M. Lifshitz, *Fluid Mechanics,* 1st ed. (Pergamon, New York, 1959).

[7] P. Huerre and P. A. Monkewitz, J. Fluid Mech. **159**, 151 (1985).

[8] S. A. Thorpe, J. Fluid Mech. **46**, 299 (1971).

[9] J. Lin, J. D. Paul, and J. P. Gollub, J. Fluid Mech. (to be published); J. Lin and J. P. Gollub, Phys. Rev. Lett. **70**, 2289 (1993).

[10] G. S. Triantafyllou, K. Kupfer, and A. Bers, Phys. Rev. Lett. **59**, 1914 (1987).

[11] H. A. Snyder, Proc. R. Soc. London, Ser. A **265**, 198 (1962).

[12] S. Chandrasekhar, Proc. R. Soc. London, Ser. A **265**, 188 (1962).

[13] K. Bühler, Z. Angew. Math. Mech. **64**, 180 (1984).

[14] K. Bühler, Strömungsmech. Strömungmach. **34**, 67 (1984).

[15] K. Bühler and F. Polifke in *Nonlinear Evolution of Spatiotemporal Structures in Dissipative Continuous Systems,* Vol. 225 of *NATO Advanced Study Institute, Series B: Physics,* edited by F. Ausse and L. Kramer (Plenum, New York, 1990), p. 21.

[16] D. I. Takeuchi and D. F. Jankowski, J. Fluid Mech. **102**, 101 (1981).

[17] B. S. Ng and E. R. Turner, Proc. R. Soc. London Ser. A **382**, 83 (1982).

[18] A. Tsameret and V. Steinberg, Europhys. Lett. **14**, 331 (1991).

[19] A. Tsameret and V. Steinberg, Phys. Rev. Lett. **67**, 3392 (1991).

[20] K. L. Babcock, G. Ahlers, and D. S. Cannell, Phys. Rev. Lett. **67**, 3388 (1991).

[21] K. L. Babcock, D. S. Cannell, and G. Ahlers, Physica D **61**, 40 (1992).

[22] M. C. Cross, Phys. Rev. A **38**, 3593 (1988); Phys. Rev. Lett. **57**, 2935 (1986).

[23] G. I. Taylor, Philos. Trans. R. Soc. London, Ser. A **223**, 289 (1923); **157**, 546 (1936).

[24] R. C. DiPrima and H. L. Swinney, *Hydrodynamic Instabilities and Transitions to Turbulence,* edited by H. L. Swinney and J. P. Gollub (Springer, Berlin, 1981); R. Graham and J. A. Domaradski, Phys. Rev. A **26**, 1572 (1982).

[25] A. Recktenwald and M. Lücke (private communication).

[26] *g* was taken to be 0.7, from the calculation for convection with axial flow (Ref. [35]).

[27] M. C. Cross and K. Kim, Phys. Rev. A **37**, 3909 (1988).

[28] G. Dee and J. S. Langer, Phys. Rev. Lett. **50**, 383 (1983); E. Ben Jacob, H. Brand, G. Dee, L. Kramer, and J. S. Langer, Physica D **14**, 348 (1985).

[29] K. Nozaki and N. Bekki, Phys. Rev. Lett. **51**, 2171 (1983); J. Fineberg, E. Moses, and V. Steinberg, Phys. Rev. A **38**, 4939 (1988).

[30] W. v. Saarloos, Phys. Rev. A **37**, 211 (1988).

[31] *CRC Handbook of Chemistry and Physics,* 65th ed. (CRC, Boca Raton, FL, 1984), Sec. D, p. 235.

[32] M. A. Dominguez-Lerma, D. S. Cannell, and G. Ahlers, Phys. Rev. A **34**, 4956 (1986).

[33] R. M. Heinrichs, D. S. Cannell, G. Ahlers, and M. Jefferson, Phys. Fluids **31**, 250 (1988).

[34] Kalliroscope Co., P.O.B. 60, Groton, MA 01450, rheoscopic liquid AQ-1000.

[35] M. A. Domingues-Lerma, Ph.D. thesis, University of California, Santa Barbara, 1986 (unpublished).

[36] H. W. Müller, M. Lücke, and M. Kamps, Europhys. Lett. **10**, 451 (1989); Phys. Rev. A **45**, 3714 (1992).

[37] A. Tsameret, G. Goldner, and V. Steinberg, Phys. Rev. E **49**, 1309 (1994).

[38] W. H. Press, B. P. Flannery, S. A. Teukolsky, and W. T. Vetterling, *Numerical Recipes in C* (Cambridge University Press, Cambridge, England, 1988).

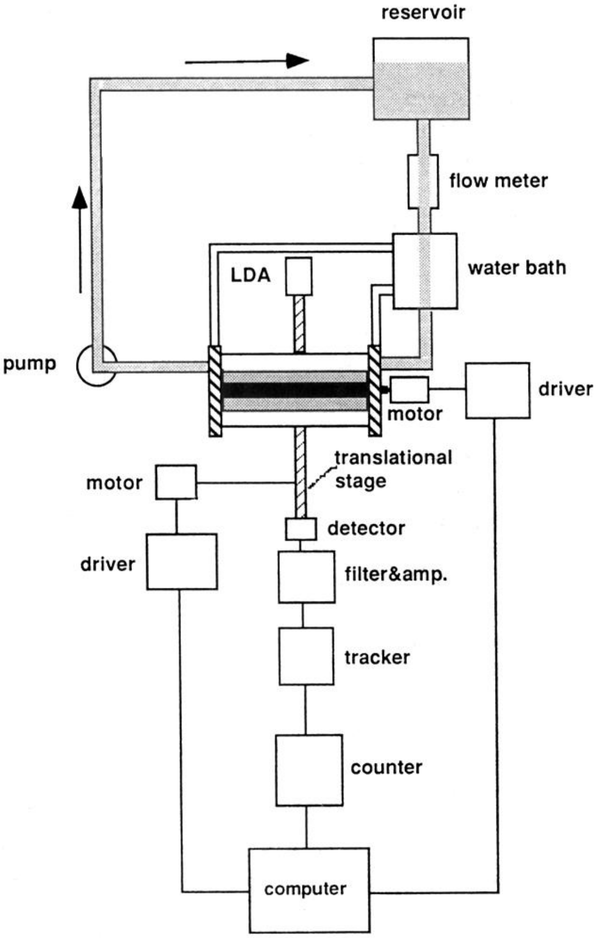

FIG. 1. The experimental setup. LDA stands for the laser Doppler anemometer.